The Astrophysical Journal, 905:1 (12pp), 2020 December 10 https://doi.org/10.3847/1538-4357/abbe06

Kinetic Simulations of Cosmic-Ray-modified Shocks. I. Hydrodynamics

Colby C. Haggerty and Damiano Caprioli
Department of Astronomy and Astrophysics, University of Chicago, 5640 S Ellis Avenue, Chicago, IL 60637, USA; chaggerty@uchicago.edu
Received 2020 September 2; revised 2020 October 1; accepted 2020 October 2; published 2020 December 7

Abstract

Collisionless plasma shocks are efficient sources of nonthermal particle acceleration in space and astrophysical systems. We use hybrid (kinetic ion—fluid electron) simulations to examine the nonlinear feedback of the self-generated energetic particles (cosmic rays, CRs) on the shock hydrodynamics. When CR acceleration is efficient, we find evidence of both an upstream precursor, where the inflowing plasma is compressed and heated, and a downstream postcursor, where the energy flux in CRs and amplified magnetic fields play a dynamical role. For the first time, we assess how nonlinear magnetic fluctuations in the postcursor preferentially travel away from the shock at roughly the local Alfvén speed with respect to the downstream plasma. The drift of both magnetic and CR energy with respect to the thermal plasma substantially increases the shock compression ratio with respect to the standard prediction, in particular exceeding 4 for strong shocks. Such modifications also have implications for the spectrum of the particles accelerated via diffusive shock acceleration, a significant result detailed in a companion paper.

Unified Astronomy Thesaurus concepts: Plasma physics (2089); Plasma astrophysics (1261); Shocks (2086); Supernovae (1668); Supernova remnants (1667); Cosmic rays (329); Galactic cosmic rays (597)

1. Introduction

Nonrelativistic shocks are abundant in space and astrophysical systems, such as the Earth's bow shock, interplanetary shocks associated with coronal mass ejections, supernovae (SNe) and supernova remnants (SNRs), and galaxy clusters; they are typically associated with nonthermal particles and emission. Such shocks occur on length scales where collisions are too infrequent to efficiently dissipate the energy flux; in fact, they are referred to as collisionless shocks because the energy dissipation is regulated by the collective interactions between the charged particles and the electromagnetic fields. Despite this, much of our understanding and predictions for the macroscopic structure of plasma shocks comes from the (collisional) fluid Rankine–Hugoniot jump conditions, which cannot accurately model the dynamics of nonthermal particles and magnetic fields. Nonrelativistic shocks can transfer as much as 10%—20% of their ram energy into energetic particles (hereafter, cosmic rays, CRs), through repeated first-order Fermi reflections, a process referred to as diffusive shock acceleration (DSA; Krymskii 1977; Axford et al. 1978; Bell 1978; Blandford & Ostriker 1978). Additionally, CRs drive plasma instabilities upstream of the shock, which amplify magnetic fluctuations and produce turbulent, large-amplitude magnetic fields, which are further compressed in the downstream region (e.g., Skilling 1975; Bell 2004; Bykov et al. 2013; Caprioli & Spitkovsky 2013, 2014b).

Previous theoretical works have included CRs in modeling the hydrodynamics of collisionless plasma shocks using a two-fluid theory (e.g., Drury & Völk 1981a, 1981b; Berezhko & Ellison 1999), an analytical kinetic theory (e.g., Eichler 1979, 1984, 1985; Ellison & Eichler 1985; Malkov 1997; Malkov et al. 2000; Blasi 2002, 2004; Amato & Blasi 2005, 2006; Caprioli et al. 2009b, 2010, 2009a), and Monte Carlo numerical approaches (e.g., Ellison & Eichler 1984, 1985; Ellison et al. 1990, 1995, 1996; Ellison & Double 2002; Vladimirov et al. 2006). Further numerical approaches have also been employed to understand the time dependence of this effect on different astrophysical shocks (e.g., Bell 1987; Jones & Ellison 1991; Berezhko & Völk 1997; Berezhko & Ellison 1999; Gieseler et al. 2000; Kang et al. 2002; Berezhko & Völk 2004; Kang & Jones 2005, 2006; Völk et al. 2005; Berezhko & Völk 2006; Zirakashvili et al. 2008; Zirakashvili & Ptuskin 2008; Zirakashvili & Aharonian 2010; Kang et al. 2013). For detailed reviews of CR-modified shocks, readers can refer to Drury (1983), Blandford & Eichler (1987), Jones & Ellison (1991), and Malkov & Drury (2001).

When even a relatively small fraction of shock energy ($\sim$10%) is channeled into CRs, an upstream precursor is formed and the speed and compressibility of the shock are affected at the zeroth order. The standard prediction is that the CR contribution should lead to a larger total shock compression ratio, possibly as large as 10–100 for strong shocks (e.g., Drury 1983; Jones et al. 2001; Malkov & Drury 2001). The effect of self-generated, amplified magnetic fields has been predicted to limit such a compression to values $\lesssim$10 (Vladimirov et al. 2006; Caprioli et al. 2008, 2009a), but always greater than the fiducial value of 4 for shocks with Mach number $\gg$1. While there is general agreement that self-generated CRs and magnetic fluctuations should modify the hydrodynamics of a shock, the process through which this occurs has not yet been assessed from first principles.

In this paper we present the first numerical evidence of CR-modified shocks in ab initio plasma simulations in the hybrid limit (kinetic ions–fluid electrons). We detail how CRs and CR-driven magnetic fluctuations affect the hydrodynamics of the shock, while in a companion paper, Caprioli et al. (2020), we discuss how the modified hydrodynamics affect the spectrum of the particles accelerated via DSA.

The layout of this paper is as follows: in Section 2, we detail the hybrid code and the shock simulation setup. In Sections 3 and 4, we identify and discuss the formation of a precursor region in the upstream and a postcursor region in the downstream, respectively. In Section 5, we present CR-modified shock jump conditions and show they are in good agreement with simulations. Finally, in Section 6, we discuss the implication of these corrections to the fluid dynamics of collisionless plasma shocks.

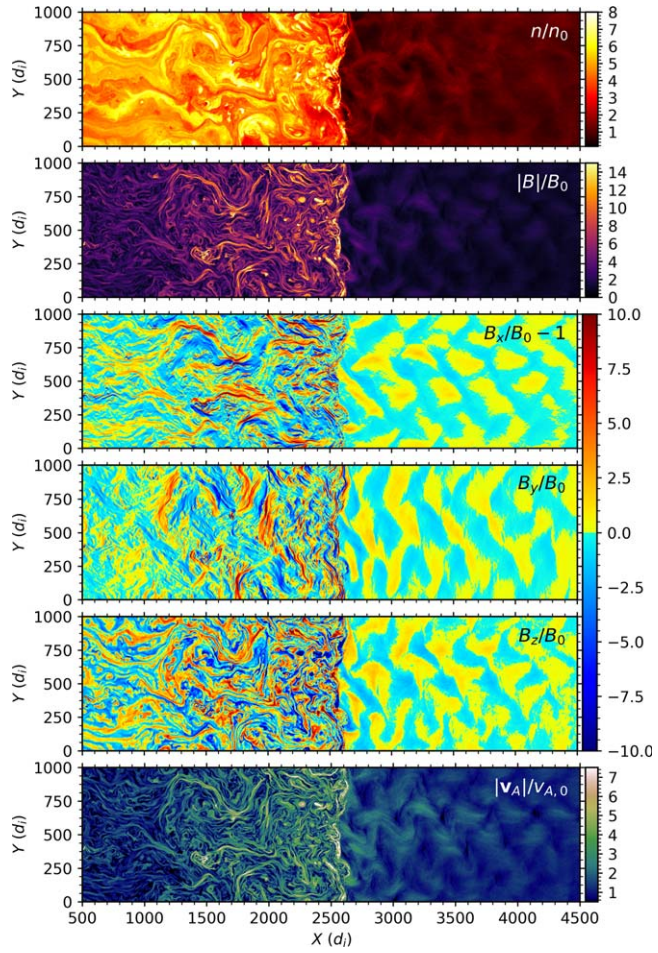

Figure 1. 2D snapshot of an $M = 20$ parallel shock at time $t = 500\Omega_{ci}^{-1}$. Quantities are (top to bottom): density, magnitude of the magnetic field, self-generated components of the magnetic field ($B_x/B_0 - 1$, B_y, and B_z), and magnitude of the local Alfvén speed $|\boldsymbol{v}_A| = |\boldsymbol{B}|/\sqrt{4\pi m_i n}$. The shock is at $x \sim 2500 d_i$.

2. Hybrid Simulations

To study the nonlinear effects of self-generated CRs on the hydrodynamics of the shock, we perform self-consistent simulations using dHybridR, a relativistic hybrid code with kinetic ions and (massless, charge-neutralizing) fluid electrons (Haggerty & Caprioli 2019). dHybridR is the generalization of the Newtonian code *dHybrid* (Gargaté et al. 2007), which has been already widely used for simulating collisionless shocks (Gargaté & Spitkovsky 2012; Caprioli & Spitkovsky 2014a, 2014b, 2014c; Caprioli et al. 2015, 2017, 2018; Haggerty et al. 2019; Caprioli & Haggerty 2019). Hybrid codes are better suited to self-consistently simulate the long-term shock evolution than full particle-in-cell (PIC) codes because they do not need to resolve the small time/length scales of the electrons, which are usually dynamically negligible (see, e.g., Winske 1985; Quest 1988; Scholer 1990; Giacalone et al. 1992, 1993; Bennett & Ellison 1995; Winske & Omidi 1996; Giacalone et al. 1997; Giacalone & Ellison 2000; Lipatov 2002; Giacalone 2004; Burgess et al. 2005; Guo & Giacalone 2013; Burgess et al. 2016; Kropotina et al. 2016; Hanusch et al. 2019, and references therein).

All physical quantities are normalized to their far upstream values, namely, mass density to $\rho_0 \equiv m_i\, n_0$ (with m_i the ion, namely, proton, mass), magnetic fields to B_0, lengths to the ion inertial length $d_i = c/\omega_{pi}$ (with c the speed of light and ω_{pi} the ion plasma frequency), time to the inverse ion cyclotron frequency Ω_{ci}^{-1}, and velocity to the Alfvén speed $v_{A,0} = B_0/\sqrt{4\pi\rho_0}$. The ion temperature is chosen such that the thermal gyroradius is 1 d_i, corresponding to an ion thermal to magnetic pressure ratio of $\beta_i = 2$. The system is 2D in real space (in the $x - y$ plane), and all three components of the momenta and electromagnetic fields are retained. The hybrid model requires an explicit choice for the electron equation of state, and in this work, electrons are assumed to be adiabatic, i.e., the electron pressure is $P_e \propto \rho^{5/3}$. We remark on the motivation and consequences of choosing this equation of state in Section 6.

The simulations are initialized with a uniform magnetic field $\boldsymbol{B}_0 = B_0\boldsymbol{x}$ and with a thermal ion population with a bulk flow $\boldsymbol{v}_x = -Mv_{A,0}\boldsymbol{x}$. The simulations are periodic in the y direction, the right boundary is open and continuously injecting thermal particles, and the left boundary is a reflecting wall; after tens of cyclotron times, the ion population closest to the wall reflects, becomes unstable, and forms a shock. This shock then travels in the $+\boldsymbol{x}$ direction, parallel to the background magnetic field (*parallel shock*), with the downstream plasma at rest in the simulation reference frame. Note that M defines both sonic and Alfvénic Mach numbers $M \equiv M_A = \sqrt{\gamma}M_s$ in the downstream (simulation) frame, while the Mach number that enters the stationary jump conditions is the one in the shock frame, which is 20%–30% larger, depending on the shock compression ratio (see Section 5). Most of the analysis in this work is done on a benchmark simulation with $M = 20$ and a domain of size $[L_x, L_y] = [10^5, 200]d_i$, wide enough to account for 2D effects and long enough so that the simulation could be run for more than 1000 Ω_{ci}^{-1} without energetic particles escaping the box. The simulation has two grid cells per d_i, and each grid cell is initialized with four particles per grid. The speed of light is set to be much larger than the Alfvén and thermal speeds ($c/v_{A,0} = c/v_{thi} = 100$), as discussed in Haggerty & Caprioli (2019); the time step is set as $c\Delta t = d_i/10$.

Simulations with Mach numbers in the range $M = 10$–80 were performed; their parameters are detailed in Appendix A. All of the following analysis and figures in this work are preformed with the $M = 20$ benchmark simulation, unless stated otherwise. The choice stems from the fact that an $M = 20$ simulation is representative of a strong shock ($M \gg 1$) and can still be run for a long time without CRs escaping the simulation domain; the computational cost of a dHybridR simulation scales $\propto M^2$ when keeping the box size fixed in units of the ion gyroradius (for a Newtonian hybrid code it would scale $\propto M^3$, since dt is also inversely proportional to M if not normalized to c).

Moreover, for $M = 20$ the fastest-growing modes, driven by streaming CRs, are in the resonant regime (nonresonant modes start to become prominent for $M \gtrsim 30$; see Caprioli & Spitkovsky 2014b); this means that the amplified fields should be Alfvénic and remain quasi-linear upstream, which simplifies the theoretical interpretation. We have also performed runs with larger M (Section 5.4), for which magnetic field amplification occurs in the Bell regime, finding consistent results for all strong shocks.

A shorter $M = 20$ simulation with a wider box $L_y = 10^3 d_i$ was run for assessing convergence with the transverse size; quantities from this simulation are shown in Figure 1. With these parameters, strong parallel shocks can channel as much as 10%–15% of their

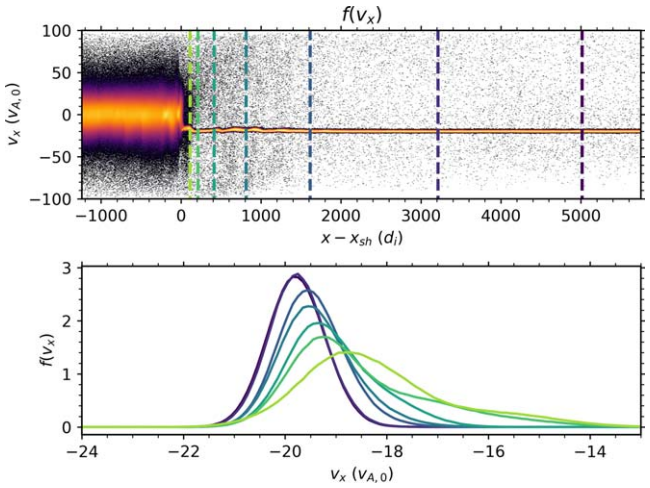

Figure 2. Top panel: ion $x - v_x$ phase space distribution function at $t = 1400\Omega_{ci}^{-1}$, with the x-axis shifted to the shock is at $x = 0$ Bottom panel: ion spectra at different upstream positions (color-coded as in the top panel); cuts are time-averaged between $t = 1350 - 1550\Omega_{ci}^{-1}$ to remove high-frequency fluctuations. The bulk speed decreases and the thermal speed increases while approaching the shock.

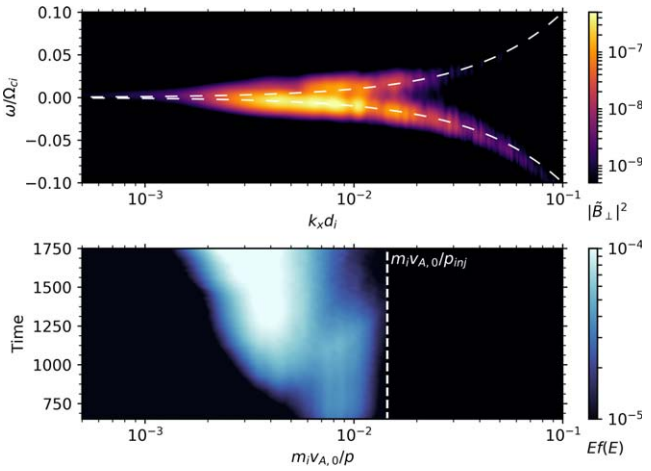

Figure 3. Top panel: power in the upstream transverse magnetic field components $|\tilde{B}_\perp|^2 \equiv |\tilde{B}_y|^2 + |\tilde{B}_z|^2$, where $\tilde{B}_i$ is the Fourier transform of $B_i(x, t)$, as a function of wavenumber (k) and angular frequency (ω). In this plot, modes with positive (negative) ω correspond to waves traveling left (right) and dashed white lines to Alfvén the phase velocity of $\pm v_{A,0}$. Self-generated modes are Alfvénic and preferentially move to the right, i.e., against the fluid. Bottom panel: the upstream CR energy spectrum, plotted in time (vertical axis) as a function of $m_i v_{A,0}/p$, which can be roughly interpreted as the resonant wavenumber. The comparison between panels highlights the quasi-resonance between the CR and wave power spectra.

kinetic energy into CRs and effectively amplify magnetic fields (Caprioli & Spitkovsky 2014a, 2014b, 2014c).

3. The Upstream Precursor

3.1. Hydrodynamics

When a large enough fraction of the shock kinetic energy and pressure are deposited into energetic particles, the standard shock hydrodynamics are altered from the ones described by the gaseous Rankine–Hugoniot jump conditions. CRs break the causality wall represented by the shock, and thus can transfer momentum and energy back upstream, effectively slowing the shock and precompressing the incoming plasma, forming a CR-induced *precursor* (e.g., Drury 1983; Jones & Ellison 1991; Blandford & Eichler 1987; Malkov & Drury 2001). For the quantities measured in this work, we use the subscripts 0, 1, and 2 for the far upstream, the precursor immediately upstream of the shock, and downstream, respectively.

The formation of the CR precursor is evident in our simulations: the upper panel of Figure 2 shows the $x - v_x$ phase space distribution function integrated/averaged over the y, v_y, and v_z directions at $1400\Omega_{ci}^{-1}$. Cuts of the ion v_x distribution are shown in the lower panel. Each cut is taken at different distances from the shock (color-coded) and averaged over $t = 1350$–$1550\Omega_{ci}^{-1}$. The bulk flow speed (i.e., the mean of the v_x distribution) upstream of the subshock is $u_1 \sim 0.9u_0$, consistent with pressure in CRs being $\sim$10% of the bulk ram pressure. In the precursor, thermal ions warm up (i.e., the v_x distributions become wider) well beyond what is predicted by adiabatic heating due to the observed compression[1] $\rho_1/\rho_0 \sim 1.09$. A temperature increase consistent with adiabatic heating would yield $T_1/T_0 = (\rho_1/\rho_0)^{2/3} \approx 1.06$, while Figure 2 indicates a much larger temperature increase, $T_1/T_0 \sim 2.7$. Such a nonadiabatic heating is due to the damping of the waves produced by CR-driven instabilities (e.g., Ellison et al. 1981; Völk & McKenzie 1981; Amato & Blasi 2006; Caprioli et al. 2009b; Tatischeff & Hernanz 2007) and corresponds to maintaining a constant thermal/magnetic pressure ratio in the shock precursor, despite the effective magnetic field amplification.

3.2. Magnetic Field Amplification

The CR population is intrinsically anisotropic in the upstream fluid frame, which leads to the development of several plasma instabilities that have been investigated theoretically and numerically in numerous works (e.g., Kulsrud & Pearce 1969; Skilling 1975; Bell 1978; Zweibel 2003; Bell 2004; Reville et al. 2008; Amato & Blasi 2009; Riquelme & Spitkovsky 2009; Reville & Bell 2013; Caprioli & Spitkovsky 2014b; Bai et al. 2019; Haggerty et al. 2019; Zacharegkas et al. 2019). The presented kinetic simulations capture self-consistently both the formation of the precursor and the CR-driven magnetic fluctuations.

The power spectrum of self-generated magnetic fluctuations in the upstream is shown in the top panel of Figure 3 for our benchmark run. The spectrum is calculated using the transverse components of the magnetic field with $|\tilde{B}_\perp|^2 \equiv |\tilde{B}_y|^2 + |\tilde{B}_z|^2$, where $\tilde{B}_i$ is the Fourier transform of $B_i(x, t)$, as a function of wavenumber k and angular frequency[2] ω. Also, it is evaluated over a relatively large window [60, 000 d_i, 200 d_i], embedded in the upstream flow, with the left side of the window beginning at $x = 23, 600\, d_i$ at $t = 600\, \Omega_{ci}^{-1}$ and ending at $x = 8000 d_i$, just in front of the shock, at $t = 1780\, \Omega_{ci}^{-1}$. The phase velocity of an Alfvén wave, based on the initial upstream magnetic field and density, is shown by the white dashed lines, with the upper and lower lines corresponding to waves traveling toward (leftward) and away from (rightward) the shock, respectively. Most of the magnetic power is in modes with phase speeds comparable to the initial upstream Alfvén speed and with $\omega < 0$, i.e., modes that are propagating *away*

[1] Mass flux conservation implies that ρu is constant.

[2] In practice, we calculate the discreet Fourier transform of $B_i(x, y, t)$ in the x and t directions, average over the y direction, and normalize to the number of grid points in x and t.

from the shock in the fluid rest frame and down the CR pressure gradient.

Furthermore, most of the power is in modes with wavenumbers between $kd_i \sim 0.002 - 0.02$, which are resonant with the CR population upstream of the shock. The distribution of the CR population can be seen in the bottom panel of Figure 3, which shows a 2D map of the ion energy spectrum, $Ef(E)$, integrated over the transformation window. The spectrum is plotted as a function of time and inverse momentum ($m_i v_{A,0}/p$), which, for a constant magnetic field strength, can be interpreted as the corresponding resonant wavenumber. Note that the CR spectrum is cut off for values smaller than the injection momentum (p_{inj}, vertical dashed line), so that the signal is not overpowered by the inflowing beam of ions with $p = 20 m_i v_{A,0}$ (Caprioli et al. 2015). By comparing the x-axis of the energy spectrum and magnetic power spectrum, it can be concluded that, for the benchmark simulation, the amplified modes are driven by the resonant CR streaming instability, (e.g., Kulsrud & Pearce 1969; Skilling 1975; Bell 1978; Zweibel 2003); this result is in agreement with theoretical expectations (Amato & Blasi 2009) and previous hybrid simulations (Caprioli & Spitkovsky 2014b), which suggest that the nonresonant (Bell) instability should become dominant only for $M \gtrsim 30$.

3.3. The Quasi-periodic Nature of the Precursor

While the standard predictions for the precursor are recovered in time-averaged simulation data, a high-cadence analysis shows that the precursor varies significantly on intermediate timescales, around $50–200\Omega_{ci}^{-1}$. These timescales roughly match the period of the Doppler-shifted Alfvénic fluctuations in the precursor.[3]

A global time variability originates from the CR-driven instabilities and the spatially inhomogeneous amplification of the upstream magnetic field. In fact, the effective shock inclination, $\vartheta_{eff}(t)$, is modulated on timescales comparable to the wave period. Furthermore, the shock inclination controls particle injection into DSA, which is more prominent for quasi-parallel shock configurations and suppressed for oblique ($\vartheta_{eff} \gtrsim 50°$) ones.

This modulation can be seen in Figure 4, where the dark green line (left axis) shows $\vartheta_{eff}(t) \equiv \cos^{-1}(\langle B_x/|B|\rangle)$, with the magnetic field averaged over a region between 350 and 450 d_i upstream of the shock. Sufficiently far upstream the field is mostly along its initial direction, but $\vartheta_{eff}(t)$ oscillates around its average of $\approx 48°$ (dashed line) with a period comparable to that of the self-generated waves.

Figure 4 also shows the transverse CR pressure, defined as $P_{yy} + P_{zz}$, where $P_{ii} = \int_{p_{inj}}^{\infty} p_i v_i f d^3p$ in units of the upstream thermal pressure P_0 (light blue, right axis), calculated over the same region as ϑ_{eff}. Such a CR pressure varies with a period comparable to the shock inclination too, but the two quantities appear to be generally anticorrelated. We conclude that CR injection, the prominence of the precursor, and the shock inclination are all modulated by the period of the waves generated via CR streaming instability in the precursor. The imprint of upstream magnetic fluctuations on the shock dynamics is expected to survive also in more realistic (much wider and 3D) systems, though as a local phenomenon that, arguably, causes shock rippling. This quasi-periodic nature of precursors may be measurable in situ at heliospheric shocks and must be reckoned with when determining the fundamental inclination of a shock based on an instantaneous measurement ϑ_{eff}.

[3] Most of the power in resonant modes are at wavelengths of $\lambda \sim 2\pi/k \sim 2000\, d_i$ (Figure 3). With a bulk flow of $\sim 20 v_{A,0}$, the period of these oscillations in the shock frame are $\sim \lambda/(20 v_{A,0}) \sim 100\Omega_{ci}^{-1}$.

4. The Downstream Postcursor

In contrast to the formation of the shock precursor, what was not predicted by any theory (that we are aware of) and what we found for the first time in self-consistent plasma simulations is the formation of a nonlinear structure downstream of the shock, which we call a *postcursor*.

The postcursor manifests itself as an extended downstream region where the self-generated magnetic fluctuations have an important dynamical role and the dynamics of thermal plasma and CRs are decoupled, in the sense that CRs and magnetic perturbations have a sizable drift speed with respect to the bulk plasma.

A standard assumption in DSA theory is that CRs are quickly isotropized in the frame of the magnetic fluctuations, usually assumed to be Alfvén waves (Skilling 1975), and that the Alfvén speed is much smaller than the flow speed in the shock frame, so that eventually CRs are isotropic in the flow frame at the order of v_A/u. Deviations from such an isotropy may arise if the shock is oblique and transrelativistic (e.g., Baring et al. 1995; Ellison et al. 1996; Bell et al. 2011) or, in general, in the presence of anisotropic transport (e.g., Kirk et al. 1996; Morlino et al. 2007).

In the presence of magnetic field amplification, the condition $v_A/u \ll 1$ may be violated: it has been suggested (Zirakashvili & Ptuskin 2008; Caprioli et al. 2009b; Caprioli 2011, 2012) that retaining the *upstream* Alfvénic drift of CRs with respect to the background fluid may also affect the resulting CR spectrum appreciably (Morlino & Caprioli 2012; Kang et al. 2013; Slane et al. 2014; Kang & Ryu 2018; Bell et al. 2019). Retaining this effect upstream is natural, since self-generated waves travel against the CR gradient, i.e., toward upstream infinity resulting in a net CR drift $v_{CR,x} \simeq u - v_A$, as shown in the top panel of Figure 3. However, it has always been assumed that *downstream* magnetic fluctuations should not have a preferential direction, hence canceling any net drift (see Skilling 1975 for a rigorous derivation of CR transport in the presence of waves of both helicities).

4.1. CR Drift Downstream

In this work we find, for the first time, evidence for a net CR drift away from the shock, as shown in Figure 5. In all the panels, the color code corresponds to time evolution. The top two panels show the bulk velocity normal to the shock, for all the ions (thermal + CRs, v_x; top panel) and for the CRs alone ($v_{CR,x}$; bottom panel). The speeds are averaged along y and shown as a function of x. The CR velocity is defined as the mean velocity of particles with momentum larger than p_{inj}, i.e.,

$$\boldsymbol{v}_{CR} \equiv \int_{p_{inj}}^{\infty} \boldsymbol{v} p^2 f dp \Big/ \int_{p_{inj}}^{\infty} p^2 f dp, \tag{1}$$

where $p_{inj} \approx \sqrt{10}\, m u_0$ according to the injection theory derived from hybrid simulations in Caprioli & Spitkovsky (2014a) and Caprioli et al. (2015).

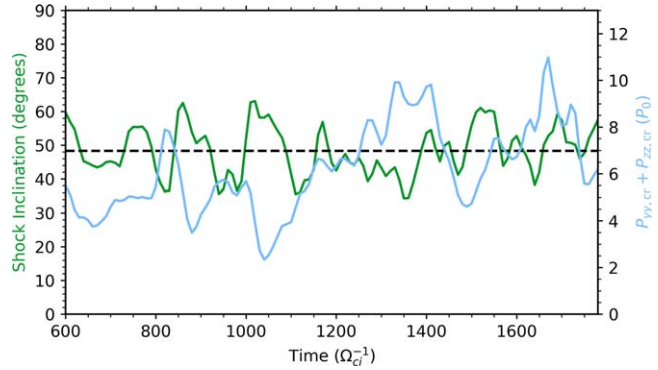

Figure 4. Angle between the magnetic field immediately upstream of the shock and the shock normal ($\vartheta_{\rm eff} = \cos^{-1}(\langle B_{x,1}/|B_1|\rangle$, left axis, green line), and total transverse CR pressure in the upstream ($P_{yy} + P_{zz}$, right axis, light blue line, normalized to $P_0 \equiv \rho_0 v_{A,0}^2$). Note the quasi-periodic behavior, with a timescale of $\sim 200\Omega_{ci}^{-1}$ and the general anticorrelation between shock inclination and CR pressure.

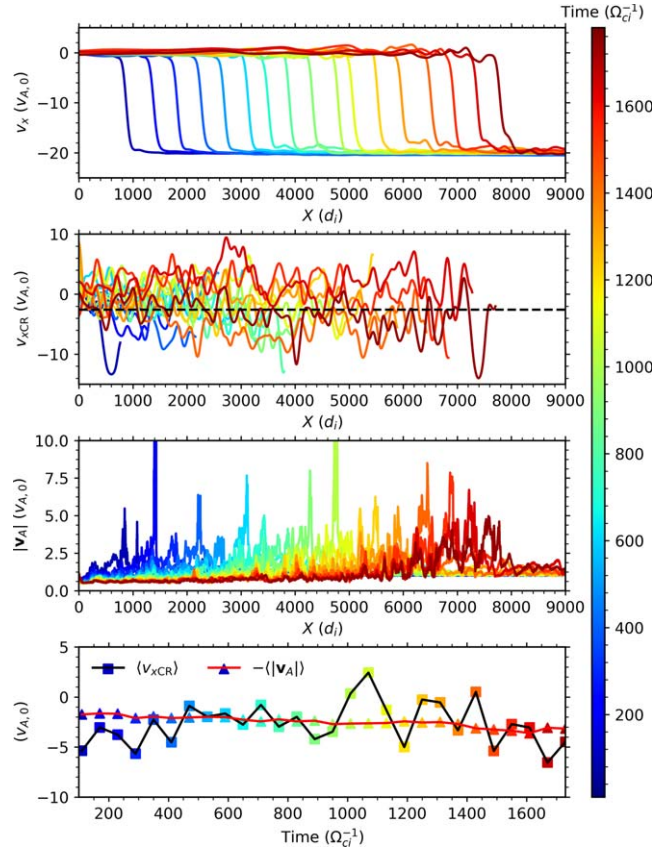

Figure 5. Time evolution of the velocity profiles, averaged over the transverse direction, for all the ions (v_x), CR only ($v_{{\rm CR},x}$; see Equation (1)), and local Alfvén speed, $|v_{\rm A}| = |\boldsymbol{B}|/\sqrt{4\pi\rho}$ (top three panels). The bottom panel compares CR (black line, squares) and Alfvén (red line, triangles) speeds averaged $500d_i$ behind the shock, suggesting that CRs drift toward the downstream with respect to the thermal plasma at speeds comparable to the local magnetic fluctuations. The horizontal dashed line marks the time-averaged postcursor Alfvén speed.

While the downstream plasma is—as expected—at rest behind the shock in the simulation frame (top panel of Figure 5), the velocity of the CR population has a net negative value of about 2–$3v_{\rm A,0}$ in the postcursor, about $500d_i$ wide just downstream, and reduces in magnitude further downstream until vanishing close to the left wall (second panel). Ultimately, the drift of CRs is controlled by their interaction with the magnetic fluctuations, and so this flux is expected to be tied to the dynamics of the downstream magnetic field.

The third panel of Figure 5 shows the local Alfvén speed $|\boldsymbol{v_A}(x)| = \langle |\boldsymbol{B}(x, y)|/\sqrt{4\pi\rho(x, y)}\rangle_y$, averaged in the y direction (see also the bottom panel of Figure 1). It is important to stress that this quantity is only informative about the typical speed of the magnetic perturbations, which are not simple Alfvén waves but rather large-amplitude structures created by CR-driven instabilities in the precursor and further compressed at the shock. In the paper we will commonly use "wave" for brevity, bearing in mind that magnetic structures are often nonlinear. Finally, the bottom panel of Figure 5 compares directly the average CR drift velocity and the postcursor Alfvén speed: they are consistently similar in time and approach $|\boldsymbol{v_A}| \approx 3v_{\rm A,0}$ at later times.

In summary, in the postcursor, the downstream CRs drift away from the shock with respect to the thermal plasma at a speed comparable to the local Alfvén speed; the extent of the CR postcursor is determined by the spatial extent of the amplified magnetic field.

4.2. Motion of Postshock Magnetic Structures

Even if there is agreement in the magnitude of CR drift and Alfvén speeds, we are left with the task to demonstrate that the frame in which CRs are isotropic is actually the wave frame. Note that in simulations we observe CRs drift *away from the shock* relative to the thermal plasma, and it is not obvious that magnetic fluctuations should have a preferred direction of propagation downstream. To quantify this, we present two distinct diagnostics: a morphological analysis of the magnetic structures behind the shock and a calculation of the wave dispersion relations.

The evolution of the magnetic field (B_z and $|\boldsymbol{B}|$) is shown in Figure 6: 1D cuts are taken along the x direction, averaged between $y = \{47.5, 52.5\}\ d_i$, and plotted from $x = 2500d_i$ to $7000d_i$ over the last $1200\Omega_{ci}^{-1}$ of the simulation. In each panel the shock front makes a nearly straight line with a positive slope corresponding to the inverse of the shock speed; the downstream region lies above this line. The inclination of the postshock, finger-like, magnetic structures provides an estimate of their velocity in the simulation frame: just behind the shock, waves have a negative velocity consistent with dashed lines of $-2.5v_{\rm A,0}$, while further downstream they are almost at rest (i.e., vertical). This suggests that, in the postcursor, magnetic fluctuations are traveling *away* from the shock faster than the thermal plasma, consistent with the net CR drift.

The Fourier analysis of the postshock magnetic structures shown in Figure 7 also supports this claim. The transform is calculated the same as in Figure 3, and over the last $1200\Omega_{ci}^{-1}$ of the simulation, in a window $[500\ d_i, 200d_i]$, positioned just downstream and moving with the shock; the angular frequency versus wavenumber diagram is then boosted back into the downstream frame. Most of the power is in modes with $\omega > 0$, i.e., modes that move away from the shock with respect to the background plasma, at speeds ranging between $-4v_{\rm A,0}$ and $-1v_{\rm A,0}$, corresponding to the different dashed lines in Figure 7 and consistent with the 2D time stack plots in Figure 6.

While the dispersion relationship is not as clear as Figure 3, due to the nonlinear nature of the modes, we can still conclude that the postcursor magnetic structures preferentially move away from the shock, with phase speeds consistent with the

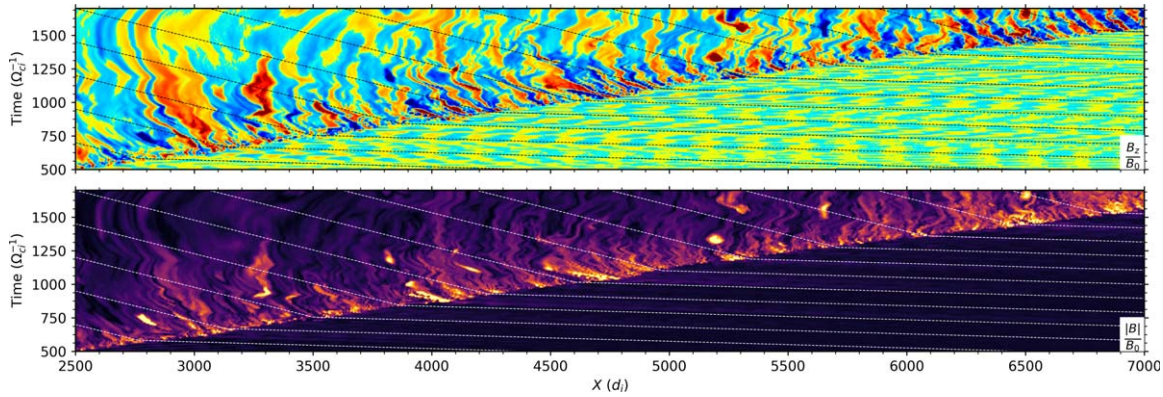

Figure 6. Evolution of the simulation magnetic field. At any given time, a 1D cut is plotted (averaged on $5d_i$ around $y = 50d_i$) for B_z and $|\boldsymbol{B}|$ (top and bottom). The diagonal dashed lines correspond to average bulk flow + Alfvén speed in the upstream and postcursor. Immediately behind the shock, the magnetic structures align with such lines, which means that the phase motion of such structures points away from the shock; further downstream, the structures are more vertical, i.e., at rest in the fluid frame.

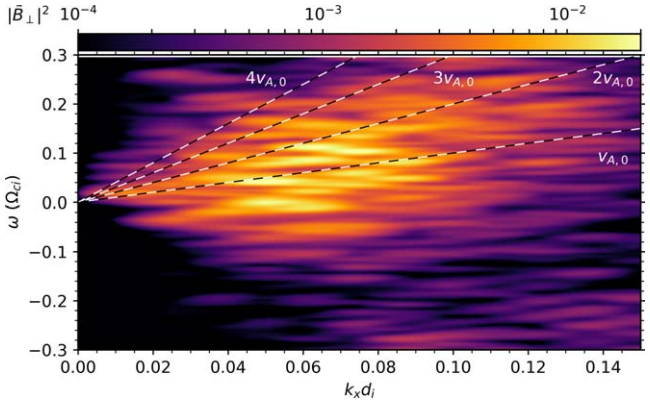

Figure 7. Magnetic power spectrum (as in Figure 3) calculated $500d_i$ downstream of the shock, over the last $1200\Omega_{ci}^{-1}$ of the simulation. Most of the power is in modes traveling away from the shock (to the left, with $\omega > 0$); the dashed lines indicate different negative integer values of $v_{A,0}$, between -1 and -4, consistent with Figure 5.

Alfvénic and CR drift speeds in Figure 5. We point out that accounting for standard reflection/transmission of the quasi-linear Alfvén waves observed upstream (Scholer & Belcher 1971) would return modes with $\omega < 0$ in the downstream, instead. Most likely, the failure of such a linear theory is due to the nonlinear, collective, reaction of the shock transition itself to the hammering of the upstream fluctuations. The shock would therefore behave as an antenna that sends magnetic perturbations toward downstream, at a speed comparable to the "natural" speed for a magnetized plasma, namely, the Alfvén speed.[4]

From all of these diagnostics a picture arises where magnetic structures generated upstream, via CR-driven instabilities, are advected and compressed through the shock and retain their inertia over a sizable region downstream, forming the postcursor. In the postcursor both the magnetic fluctuations and the CRs, which are isotropized in the wave frame, drift away from the shock faster than the thermal plasma, with a velocity on the order of the local Alfvén speed, $v_{A,2}$. Since the postshock magnetic pressure may become of order $\lesssim$10 of the shock bulk ram pressure, such a drift is *not negligible* with respect to the downstream fluid velocity; for our benchmark run, $v_{A,2} \sim 0.5u_2$.

[4] We thank S. Schwartz for pointing out such an analogy.

This extra energy flux in both energetic particles and magnetic fields behind the shock affects the shock hydrodynamics at the zeroth order. We present a discussion of the modifications to standard Rankine–Hugoniot jump conditions necessary to account for this nonlinear feedback in the next section.

5. Modified Shock Hydrodynamics

5.1. Theory

In the previous sections, we have illustrated the appearance of two nonlinear features in the shock profile: the precursor and the postcursor. Here we address how they modify the shock compression and how energy is partitioned among different components; for the effects that such modifications have on the spectrum of the accelerated particles, we refer to the companion paper, Caprioli et al. (2020).

Several works have developed a theory of CR-modified shocks including the dynamical role of energetic particles (e.g., Drury 1983; Jones & Ellison 1991; Malkov & Völk 1996; Malkov & Drury 2001; Blasi 2002; Amato & Blasi 2005, 2006; Caprioli et al. 2010; Caprioli 2012), as well as of the self-generated magnetic field (e.g., Vladimirov et al. 2006; Caprioli et al. 2008, 2009b; Slane et al. 2014), but all of these studies only accounted for the CR precursor. The main effect of the precursor is to produce a weaker subshock with compression ratio $R_{\rm sub} \equiv u_1/u_2 < 4$ and a total compression ratio $R_{\rm tot} \equiv u_0/u_2 > 4$. The actual value of the total compression ratio depends on 1) the softer equation of state of CRs, which have an effective adiabatic index of $\gamma_c = 4/3$; and 2) the escape of CRs from far upstream, which makes the shock behave as partially radiative (e.g., Drury & Völk 1981a; Jones & Ellison 1991; Caprioli et al. 2009a). The former effect would saturate the total compression to 7, but with CR escape, $R_{\rm tot}$ may become very large.

To understand the role of the postcursor, we consider the conservation equations for mass, momentum, and energy in a 1D, nonrelativistic, stationary, shock:

$$[\rho u] = 0, \tag{2}$$

$$[\rho u^2 + P_g + P_c + P_B] = 0, \tag{3}$$

$$\left[\frac{1}{2}\rho u^3 + F_g + F_c + F_B\right] = 0, \tag{4}$$

where γ_i, $_{Pi}$, and F_i are the adiabatic index, pressure, and energy flux of thermal gas, CRs, and magnetic fields ($i = g, c, B$, respectively). We define the bulk flow velocity as $\boldsymbol{u} \equiv -u\boldsymbol{x}$, such that both $u > 0$ and $F > 0$ even if $\boldsymbol{x}$ points from downstream to upstream, as in the simulations; the square brackets denote the difference between two arbitrary x locations. With appropriate prescriptions for F_i, this set of equations can be used to solve for the shock jump conditions.

The thermal gas energy flux has the canonical form:

$$F_g(x) = \frac{\gamma_g}{\gamma_g - 1} u(x) P_g(x), \tag{5}$$

and the CR energy flux is linked to the CR pressure in a similar way, i.e.,

$$F_c(x) = \frac{\gamma_c}{\gamma_c - 1} u_c(x) P_c(x), \tag{6}$$

where u_c is the CR bulk speed, including drifts. Typically, most of the CR energy is in relativistic particles and $\gamma_c \approx 4/3$, but for ab initio simulations of nonrelativistic shocks, nonrelativistic CRs carry a sizable fraction of the energy (Haggerty & Caprioli 2019); in our benchmark run, we measure γ_c as the ratio of the enthalpy density to internal energy density and obtain $\gamma_c \approx 1.5$ (see Appendix C for more details).

The "magnetic" energy flux, in general, has contributions from both the magnetic pressure and the kinetic energy associated with the plasma fluctuations, which for Alfvénic fluctuations reads (Scholer & Belcher 1971; Vainio & Schlickeiser 1999; Caprioli et al. 2009b):

$$F_B(x) = [2u_B(x) + u(x)] P_B(x), \tag{7}$$

where $u_B = u \pm v_A$ is the local velocity of the magnetic fluctuations. Equation (7) encompasses the effective equation of state for the magnetic fluctuations, which, in general, cannot be expressed as polytropic; such an equation of state depends on the nature of the fluctuations, and Equation (7) strictly holds only for Alfvénic perturbations. In the absence of a general theory, we adopt the same prescription, even when nonresonant modes dominate, relying on the fact that in its nonlinear stage, Bell-driven turbulence looks quasi-Alfvénic (Riquelme & Spitkovsky 2009; Gargaté et al. 2010; Caprioli & Spitkovsky 2014b).

Using the results from Figures 3 and 7, we have that in the precursor $u_B \simeq u - v_A$ and in the postcursor $u_B \simeq u + v_A$; far upstream $u_{B,0} \simeq u_0$ because waves have no preferential direction.

Considering Equations (3) and (4) between 0 (far upstream) and 2 (postcursor), we normalize the momentum (energy) flux equation by dividing by the ram pressure (energy) $\rho_0 u_0^2$ ($\rho_0 u_0^3/2$), introduce the normalized pressure $\xi_i \equiv P_{i,2}/(\rho_0 u_0^2)$ and $\eta_i \equiv 2\gamma_i/(\gamma_i - 1)$, obtaining

$$\xi_g \simeq 1 + \frac{1}{\gamma_g M_s^2} + \frac{1}{2M_A^2} - \frac{1}{R_{\rm tot}} - \xi_c - \xi_B \tag{8}$$

and

$$1 + \frac{\eta_g}{\gamma_g M_s^2} + \frac{3}{M_A^2} \simeq \frac{1}{R_{\rm tot}^2} + \frac{\eta_g \xi_g}{R_{\rm tot}} + \frac{u_{c,2}}{u_2}\frac{\eta_c \xi_c}{R_{\rm tot}} + \left(\frac{2u_{B,2}}{u_2} + 1\right)\frac{2\xi_B}{R_{\rm tot}}, \tag{9}$$

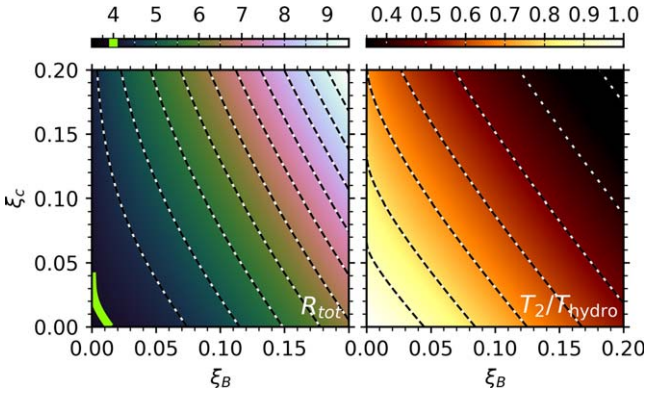

Figure 8. Prediction from the CR-modified jump conditions (Equation (B1)) for the total compression ratio ($R_{\rm tot}$, left panel) and the downstream temperature normalized to the unmodified prediction (right). Both are shown as a function of normalized downstream magnetic and CR pressures, ξ_B and ξ_c. This solution is for $M_s \approx M_A \approx 20$, as in our benchmark simulation (Section 2), but generally holds for strong shocks. The lime-green line marks the fiducial $R_{\rm tot} = 4$ prediction for strong gaseous shocks.

where $M_s^2 \equiv \rho_0 u_0^2/\gamma_g P_0$ and $M_A^2 \equiv 4\pi\rho_0 u_0^2/B_0^2$ are the far upstream sonic and Alfvénic Mach numbers, respectively. Both the far upstream CR pressure and escape flux are negligible with respect to all the other terms for moderate ξ_c (see Caprioli et al. 2009a for a detailed discussion), so we pose both $P_{c,0} \simeq 0$ and $F_{c,0} \simeq 0$.

As we saw in Section 4, $u_{B,2} \simeq u_{c,2} \simeq u_2 + v_{A,2}$, and hence

$$u_{c,2} \simeq u_{B,2} = u_2(1 + \alpha), \tag{10}$$

where $\alpha \equiv v_{A,2}/u_2$. It is useful to write α as

$$\alpha = \sqrt{2R_{\rm tot}\xi_B}. \tag{11}$$

Equations (8)–(10) can be rearranged into one equation for $R_{\rm tot}$ as a function of M_s, M_A, and the postshock pressures ξ_c and ξ_B. This equation—Equation (B1), detailed in Appendix B—is quartic with respect to $\sqrt{R_{\rm tot}}$ and its physical solution is shown in the left panel of Figure 8, where $R_{\rm tot}$ is plotted as a function of ξ_B and ξ_c, for the values of M_s, M_A, and η_c from our fiducial simulation. The striking conclusion from Figure 8 is that, even if just a few percent of the pressure is channeled into CRs and magnetic fields, $R_{\rm tot}$ becomes larger than the test-particle prediction of 4 (light-green line). Note that, in contrast to the standard nonlinear DSA theory without the postcursor, $R_{\rm tot} \gtrsim 4$ can be realized even if CRs are nonrelativistic ($\gamma_c = 5/3$) and do not escape upstream (see upper left panel of Figure 11 in Appendix B).

In fact, on top of the usual compressibility enhancement due to the presence of both CRs and magnetic field, which have a softer equation of state than the thermal gas, a key role is played by the drift of the nonthermal components in the postcursor, which effectively acts as an energy sink. Note that $R_{\rm tot}$ is more sensitive to ξ_B than ξ_c, as the amplified magnetic field contributes to both the nonthermal energy downstream as well as the rate at which both CR and magnetic energy travel away from the shock.

These nonlinear effects reduce the kinetic energy that is dissipated into heat at the shock. This can be seen in the right panel of Figure 8, which shows the fractional reduction in the downstream temperature, $T_2/T_2(\xi_B = \xi_c = 0)$, as a function of ξ_B and ξ_c for the values of M_s, M_A, and η_c from our fiducial simulation. Again, even if relatively little energy is diverted to the CRs and magnetic fields, the predicted downstream temperature can decrease by as much as 50%.

5.2. Simulation Comparison

Let us now compare the prediction for $R_{\rm tot}$ from the modified jump conditions with our benchmark simulation. First of all, we need to find the (instantaneous) shock speed and boost all the velocities in that frame, which is the only stationary frame in which Equations (2) through (4) are valid; this defines the actual value of $u_0 = Mv_{\rm A,0} + |\boldsymbol{v}_{\rm sh}| = Mv_{\rm A,0} + u_2$ used for normalization purposes, i.e.,

$$u_0 = \frac{MR_{\rm tot}}{R_{\rm tot} - 1} v_{\rm A,0}. \tag{12}$$

As in Section 4, we calculate ξ_c and ξ_B by averaging over a region $500d_i$ long behind the shock; the CR pressure is obtained by taking the appropriate moment of the ion distribution function above $p_{\rm inj}$ in the downstream frame[5]:

$$\xi_c = \frac{4\pi}{3\rho_0 u_0^2} \int_{p_{\rm inj}}^{\infty} v(p) f(p) p^3 dp. \tag{13}$$

ξ_c and ξ_B are plotted as a function of time in the first panel of Figure 9 (crosses and stars, respectively); the color code corresponds to the time in the simulation. Together, the normalized CR and magnetic pressure make up about 15%–20% of the pressure budget in the postcursor region. ξ_c increases quickly to a value just above 0.1 and remains nearly constant throughout the simulation, whereas the magnetic pressure rises more slowly up to a value of 0.05–0.075 toward the end of the simulation. The order of magnitude of the normalized pressures in the simulation makes it clear that, based on the predictions from the modified jump condition in Equation (B1), the total compression ratio should be larger than 4. The second panel of Figure 9 shows the y-averaged density profile as a function of time: at early times (blue lines) the compression ratio $R_{\rm tot} \approx 4$, but it increases with time up to $R_{\rm tot} \gtrsim 5 - 6$ toward the end of the simulation (red lines).

The agreement between the prediction based on the modified jump conditions and the simulation can be quantified by determining a time-dependent $R_{\rm tot}(t)$, averaged over the postcursor. The solution of Equation (B1) for the actual values of $\xi_c(t)$ and $\xi_B(t)$ (top panel) is compared with the measured value of $R_{\rm tot}$ (diamonds) in the bottom panel of Figure 9; the gray shaded area corresponds to a fiducial 10% error on the prediction that encompasses the uncertainty in measuring pressures and velocities in a profile with small-scale spatial variation, as well as the assumption of Alfvénic-like magnetic turbulence (Equation (7)). We find a general agreement between theory and simulations in the value, trend, and periodic variation of $R_{\rm tot}$, with minor deviations that can potentially be attributed to time evolution (not captured by Equations (2)–(4)) and transient shock features. To stress the importance of the postcursor in the shock dynamics, the bottom panel of Figure 9 includes as a dashed line the prediction with no CR/magnetic drift ($u_c = u_b = u_2$). As mentioned above, CR and magnetic pressure terms alone are not sufficient to account for the strong shock modification that we observe.

The predicted values of $R_{\rm tot}$ can also account for the quasi-periodic behavior of the shock driven by the variations in ξ_b (top panel of Figure 9). Such oscillations hinge on the same precursor physics discussed in Section 3 and will be explored in greater detail in future works.

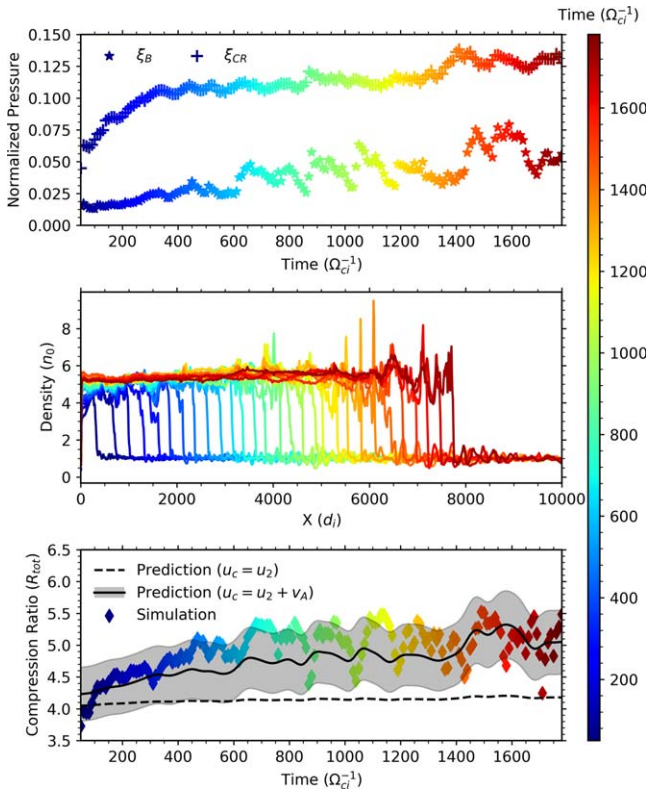

Figure 9. Time evolution (color-coded) of physical quantities that show the CR-induced modification of our benchmark shock: postcursor normalized magnetic and CR pressures, ξ_B and ξ_c (top panel), density profile (middle panel), and total compression ratio, $R_{\rm tot}$ (bottom panel). The CR pressure quickly converges to $\xi_c \approx 10\%$, while ξ_B saturates around 6%; at the same time, the compression ratio departs from the test-particle value of $\sim$4 and becomes as large as $R_{\rm tot} \gtrsim 5.5$. The prediction including the postcursor drift (Equation (B1)) is shown as a solid line with an error of 10% (gray band) and fits the simulation much better than the standard CR-modified shock prediction (dashed line).

5.3. A Critical Review of Previous Results

Such modifications on the shock hydrodynamics were not seen in previous hybrid campaigns that covered similar parameter space (Caprioli & Spitkovsky 2014a, 2014b) because of the choice of the effective electron polytropic index, γ_e. When an effective γ_e is chosen in order to mimic temperature equilibration and pressure balance between postshock electrons and ions, a large value $\gamma_e \approx 3 - 4$ must be chosen for strong shocks (see Gargaté et al. 2007; Caprioli et al. 2018 for details). However, enforcing electron–ion equilibration via an effective γ_e requires assuming a priori the value of the realized compression ratio; therefore, if one assumes that $R_{\rm tot} \approx 4$, the artificially stiff electron equation of state ends up limiting the total compression that can be achieved. Using such a prescription, Caprioli & Spitkovsky (2014a) found $R_{\rm tot} \sim 4.4$, underestimating the shock modification that we report here with the adiabatic equation of state. Note that as long as the postshock pressure does not become *dominated* by electrons (which is unphysical but may happen for $\gamma_e \gg 5/3$), the shock modification does not depend on whether electrons are adiabatic or in equipartition with the ions.

Very recently Bret (2020) pointed out how standard MHD jump conditions are not commonly realized in many papers

[5] This definition assumes that the CR distribution is isotropic in the downstream frame. This differs from the actual CR pressure on the order of $m_i v_{\rm A,2}/p_c$ where p_c is the momentum where most of the energy in the spectra resides, i.e., $p_c \sim p_{\rm inj}$ for steep spectra and in our simulation $m_i v_{\rm A,2}/p_c \sim 4\%$

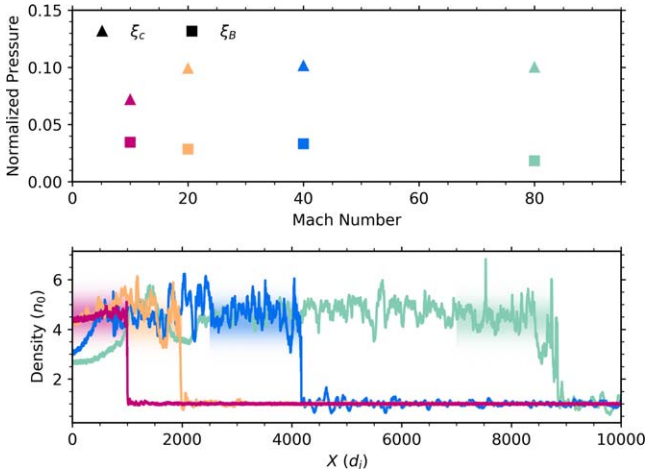

Figure 10. Top panel: normalized CR (ξ_c, triangles) and magnetic pressure (ξ_B, squares) for four different shock Mach numbers (color-coded). These values are used in Equation (B1) to predict the modified $R_{\rm tot}$ (shaded colored regions), which are compared with the actual density profiles for different M taken at $t = 375\Omega_{ci}^{-1}$ for each simulation (bottom panel). For all these strong shocks $R_{\rm tot}$ increases beyond 4, in agreement with the theory outlined here.

based on PIC simulations of shocks; our formalism, in which the kinetic backreaction of accelerated particles and self-generated magnetic fields is accounted for, naturally presents itself with a physically motivated framework in which to study the agreement between simulations and theory.

5.4. Mach Number Dependence

Beyond our benchmark $M = 20$ simulation, we have run parallel shocks with $M = 10$, 40, and 80, and the results are shown in Figure 10. As already reported by Caprioli & Spitkovsky (2014a), the normalized CR pressure—a proxy for acceleration efficiency—is generally about 10%; the normalized magnetic pressure, instead, is typically 2%–5%, values commonly inferred in multiwavelength analysis of SNRs (e.g., Völk et al. 2005; Parizot et al. 2006; Caprioli et al. 2008).

Consistent with our predictions, the shocks in each of these simulations have compression ratios that exceed the gaseous value. This enhancement is shown in the bottom panel of Figure 10, in which the y-averaged density profiles are shown. The color-coded shaded regions correspond to the prediction of $R_{\rm tot}$ from Equation (B1) and are in good agreement with the simulated values for each Mach number, which strengthens the applicability of these results to many heliospheric/astrophysical systems.

At larger Mach numbers $M \gtrsim 30$ the magnetic field amplification in the precursor is controlled by the growth of the Bell instability (e.g., Amato & Blasi 2009), whose fastest-growing modes are purely growing (i.e., with almost zero phase speed) and with wavelengths much shorter than the CR gyroradii. Nevertheless, global hybrid simulations of shocks with $M = 60$, 80, and 100 have shown that small-wavelength modes saturate rather quickly far upstream, and that in the precursor most of the power in self-generated fields is still in modes quasi-resonant with the accelerated particles (Caprioli & Spitkovsky 2014b, 2014c). In the nonlinear stage of the Bell instability waves start propagating with a phase speed close to the Alfvén speed in the amplified field (Riquelme & Spitkovsky 2009; Gargaté et al. 2010), so we expect that the general phenomenology outlined in this work should apply also at very strong shocks, such as those in SNRs.

6. Conclusions

In this work we use self-consistent hybrid simulations to study the modifications that self-generated CRs and associated magnetic turbulence induce on the dynamics of a collisionless plasma shock. The efficient acceleration of CRs leads to a precompression and deceleration of the plasma upstream of the shock: in such a precursor region, there is nonadiabatic heating of the inflowing plasma, likely a byproduct of the CR-driven magnetic fluctuations (Caprioli & Spitkovsky 2014a). Additionally, we identify quasi-periodic fluctuations in the magnetic field strength and CR pressure in the precursor, which are attributed to the shock geometry transitioning back and forth between quasi-parallel and oblique/quasi-perpendicular configurations.

Here, we report for the first time the formation of a characteristic region downstream of the shock, which we call the postcursor, where the enhanced magnetic fluctuations generated upstream and then compressed by the shock play a crucial dynamical role. Such magnetic fluctuations are found to propagate away from the shock in the downstream rest frame, with a velocity comparable to the local Alfvén speed in the amplified magnetic field (Figures 6 and 7). In the postcursor, CRs become isotropic in a frame moving with the magnetic fluctuations, rather than in the downstream fluid frame, resulting in a peculiar drift with respect to the background plasma (Figure 5).

Such nonlinear features, ultimately driven by CR physics, lead to an enhanced shock compression ratio. More precisely, the total compression ratio becomes larger than the standard value of $R_{\rm tot} = 4$, due, not only to the compressibility of relativistic CRs and magnetic fields, but mainly because of the larger rate at which the nonthermal populations are advected away from the shock, with the enhanced advection rate characterized by $\alpha = v_{\rm A,2}/u_2$. The solution of the modified jump conditions (Equation (B1)) is presented and compared with simulations proving general agreement between the predicted and measured compression ratio as a function of time (Figure 9). Even a moderate CR acceleration efficiency, $\xi_c \sim 10\%$, is able to increase the shock compression ratio for a large Mach number shock by nearly 50% from the standard fluid prediction to $R_{\rm tot} \sim 5.5$. Rewriting the advection rate as $\alpha = \sqrt{2\xi_B R_{\rm tot}}$ makes it clear that $\alpha \simeq 0.5 - 1$ for typical values of $\xi_B \sim 2 - 5\%$ and $R_{\rm tot} \sim 5 - 7$ or, equivalently, for normalized postshock magnetic energy density $\varepsilon_B = 2\xi_B$ with typical values of $\varepsilon_B \sim 5\%$–10% (e.g., Chevalier & Fransson 2006; Sarbadhicary et al. 2017; Crumley et al. 2019; Margutti et al. 2019)

We have tested that this behavior is not limited to our benchmark case by running simulations with $M = 10$, 40, and 80, which present a very similar phenomenology. While it is computationally very challenging to run kinetic simulations of strong shocks for much longer than we did, we do not see strong evolution of the shock modification in the last few hundreds Ω_{ci}^{-1} and we achieve quite large values for ξ_c and ξ_B, which may suggest that in realistic shocks the compression ratio should not be much greater than $R_{\rm tot} \gtrsim 6$. Provided that a reliable prescription for CR injection were implemented, the long-term shock evolution could be followed with hybrid +MHD codes, in which thermal particles are described as a fluid (Zachary & Cohen 1986; Lucek & Bell 2000; Reville & Bell 2012; Bai et al. 2015; van Marle et al. 2018).

The enhanced compression ratios found in these hybrid simulations can be regarded as the first ab initio evidence of the existence of CR-modified shocks, which had been suggested almost 40 yr ago (Drury & Völk 1981a, 1981b) but never verified in kinetic simulations. Observational hints of shock compression

ratios larger than 4 have been reported for young supernova remnants, such as Tycho (Warren et al. 2005) and SN1006 (Cassam-Chenaï et al. 2008); in particular, in SN1006 the distance between the forward shock and the contact discontinuity is inferred to be modulated with the azimuth, being smaller (corresponding a larger compression ratio) where the shock is quasi-parallel (see Reynoso et al. 2013), i.e., the region where CR acceleration is expected to be more prominent (Caprioli & Spitkovsky 2014a; Caprioli 2015).

The values of $\xi_c \sim 5\%$–15% and $\xi_b \sim 2\%$–10% required to produce $R_{\rm tot} \gtrsim 4$ are consistent with the values inferred from multiwavelength observations of young SNRs (e.g., Völk et al. 2005; Parizot et al. 2006; Caprioli et al. 2008; Morlino & Caprioli 2012; Slane et al. 2014), so we expect CR-induced shock modification to be a ubiquitous phenomenon.

An important result that follows from our simulations is that the main driver of the shock modification, i.e., the magnetic drift in the postcursor becoming comparable to the local Alfvén speed, can be inferred observationally. In fact, the postshock magnetic field can be constrained with nonthermal X-rays (e.g., Bamba et al. 2005; Ballet 2006; Uchiyama et al. 2007; Morlino et al. 2010; Ressler et al. 2014; Tran et al. 2015) and the gas density and temperature by X-ray (e.g., Warren et al. 2005; Miceli et al. 2012; Slane et al. 2014) and Balmer line emission (e.g., Chevalier & Raymond 1978; Ghavamian et al. 2007; Blasi et al. 2012; Morlino et al. 2013; Knežević et al. 2017), while the shock speed can be estimated from proper motion of X-ray and/or Balmer features. In principle, high-resolution X-ray observations can even test the presented theory as a function of the local shock inclination, e.g., in bilateral SNRs such as SN1006, probing whether CR-modified shocks manifest themselves in quasi-parallel regions. A corollary of our results is that quasi-perpendicular shocks, which are generally poor ion injectors (Caprioli et al. 2015, 2018), should not exhibit deviations from standard Rankine–Hugoniot conditions.

A natural question that arises is what is the spectrum of the particles accelerated in a CR-modified shock? For a dedicated discussion of such a critical question we refer to a companion paper, Caprioli et al. (2020).

We would like to thank P. Blasi, E. Amato, A. Spitkovsky, D. Eichler, L.O'C. Drury, S. Schwartz, and L. Wilson III for stimulating and constructive discussions. This research was partially supported by NASA (grant NNX17AG30G, 80NSSC18K1218, and 80NSSC18K1726), NSF (grants AST-1714658, AST-1909778, PHY-1748958, PHY-2010240), and by the International Space Science Institute's (ISSI) International Teams program. Simulations were performed on computational resources provided by the University of Chicago Research Computing Center, the NASA High-End Computing Program through the NASA Advanced Supercomputing Division at Ames Research Center, and XSEDE TACC (TG-AST180008).

Software: dHybridR(Haggerty & Caprioli 2019).

Appendix A
Simulation Details

In addition to the the benchmark $M = 20$ simulation discussed in Section 2, five simulations were performed to control for Mach number and box width. The parameters of each simulation are given in Table 1 and from left to right are simulation ID, Mach number (M), upstream ion plasma beta (β_i), simulation speed of light (c), grid size (Δx), time step (Δt), simulation length (L_x), and simulation width (L_y). Each simulation uses 16 macroparticles per d_i^2. The reduction in the box length for M80 was to compensate for the added computational cost of the reduced time step.

Table 1
Parameters for the Different Simulations Preformed and Analyzed in This Work

Sim	M	β_i	c ($v_{A,0}$)	Δx (d_i)	Δt (Ω_{ci}^{-1})	L_x (d_i)	L_y (d_i)
M10	10	2	50	0.5	0.005	10^5	200
M20	20	2	100	0.5	0.0025	10^5	200
M20w	20	2	100	0.5	0.0025	10^5	1000
M40	40	2	200	0.5	0.00125	10^5	200
M80	80	2	400	0.5	0.000625	5×10^4	200

Appendix B
The Solution to the CR-Modified Jump Conditions

The total compression ratio can be found by combining Equations (8)–(10). The equations can be rewritten into a single quartic equation in terms of $X = \sqrt{R_{\rm tot}}$ where the coefficients depend on M_s, M_A, and the postshock pressures ξ_c and ξ_B, namely,

$$c_1 X^4 + c_2 X^3 + c_3 X^2 + c_4 = 0, \tag{B1}$$

with the coefficients

$$c_1 = 1 + \frac{\eta_g}{\gamma_g M_s^2} + \frac{3}{M_{\rm A}^2}$$
$$c_2 = -\sqrt{2\xi_B}(\eta_c \xi_c + 4\xi_B)$$
$$c_3 = \eta_g\left(\xi_c + \xi_B - 1 - \frac{1}{\gamma_g M_s^2} - \frac{1}{2M_{\rm A}^2}\right) - \eta_c \xi_c - 6\xi_B$$
$$c_4 = \eta_g - 1.$$

Since $\gamma_g = 5/3$, $\eta_g = 5$, while for γ_c between $5/3$ and $4/3$, η_c varies between 5 and 8; in our benchmark simulation, $\gamma_c \simeq 1.5$ and $\eta_c \simeq 6$ (see Appendix C), which is also used for the predictions for different Mach number simulations in Figure 10. Note that it is not possible to introduce an effective adiabatic index for the wave/magnetic fields because the relationship between pressure and energy density is nontrivial even when assuming Alfvén waves (Equation (7)).

Equation (B1) has four roots, but only one of which is physically relevant. Since ξ_c, $\xi_B \ll 1$, two of the roots are negative and can be neglected. Of the two positive remaining roots, only one corresponds to an increase in density, temperature, and entropy at the shock and thus is the physical solution. Note that for non-null ξ_c and ξ_B, the trivial solution $X = 1$ disappears.

Appendix C
The CR Adiabatic Index

To correctly predict the hydrodynamic modifications, an effective adiabatic index, γ_c, must be determined for the transrelativistic CR distribution. γ_c is measured as the ratio of the enthalpy density to the internal energy density:

$$\gamma_c = 1 + \frac{\int_{p_{\rm inj}}^{\infty} vp^3 \Big/ 3f dp}{\int_{p_{\rm inj}}^{\infty} m_i c^2 (\Gamma - 1) p^2 f dp}, \tag{C1}$$

where Γ is the Lorentz factor. For nonrelativistic particles, $mc^2(\Gamma - 1) \approx pv/2$ and $\gamma_c = 5/3$, while for relativistic

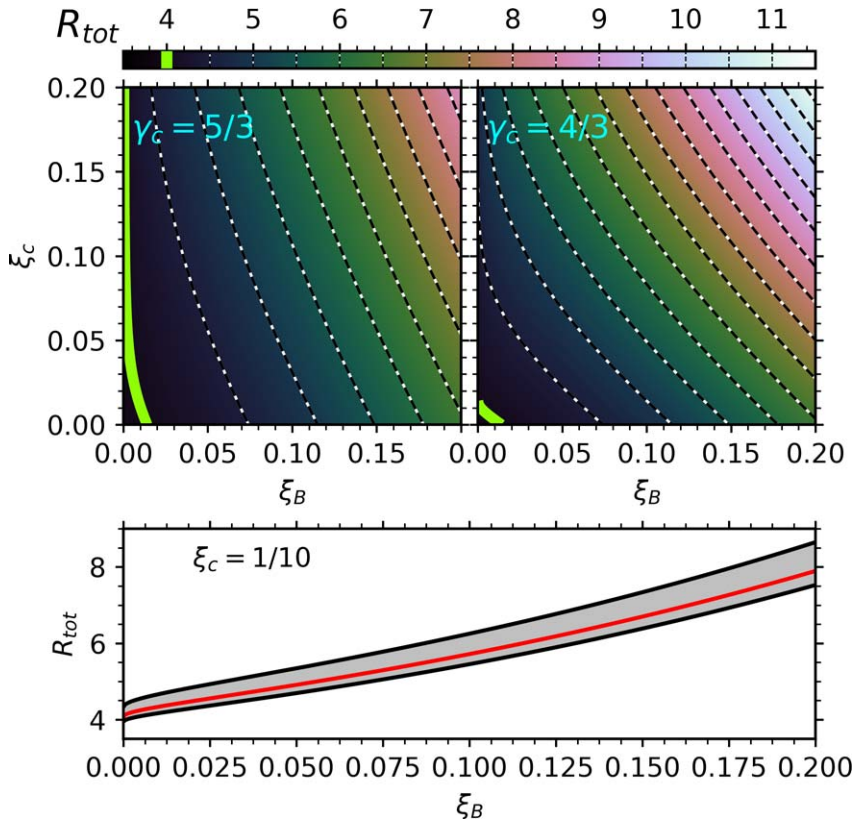

Figure 11. Top panels: total compression ratio, $R_{\rm tot}$, calculated from the modified jump conditions (Equation (B1)) for nonrelativistic ($\gamma_c = 5/3$; left) and ultrarelativistic CRs ($\gamma_c = 4/3$; right). Both are calculated with $M_s \approx M_{\rm A} \approx 20$ as in our benchmark simulation and shown as a function of normalized downstream magnetic and CR pressures, ξ_B and ξ_c. The lime-green line marks the fiducial $R_{\rm tot} = 4$ prediction for strong gaseous shocks. A 1D cut of these solutions is shown in the bottom panel, varying ξ_B for constant $\xi_c = 0.1$. The shaded region is bound by the nonrelativistic and ultrarelativistic cases, and the solution using the measured $\gamma_c = 1.5$ is shown by the red line.

distributions, $mc^2(\Gamma - 1) \approx pc$, yielding $\gamma_c = 4/3$. In general, the exact value for the γ_c will depend on the CR distribution function, but will be bounded by these two values. The top panels of Figure 11 show the upper and lower bounds for the solution for $R_{\rm tot}$ based on Equation (B1). In both the nonrelativistic (left) and relativistic (right) cases, we obtain $R_{\rm tot} \gtrsim 4$ even for modest values of ξ_B and ξ_c; in general, $R_{\rm tot}$ is larger in the relativistic case. To further illustrate the effect of the CR equation of state, the predicted compression ratio for a fixed value of $\xi_c = 0.1$ and varying ξ_B are shown in the bottom panel of Figure 11; varying the CR adiabatic index modifies $R_{\rm tot}$ by about 10% at most, an effect less important than the one induced by the CR drift in the precursor, which is controlled by ξ_B.

ORCID iDs

Colby C. Haggerty https://orcid.org/0000-0002-2160-7288

References

Amato, E., & Blasi, P. 2005, MNRAS, 364, L76
Amato, E., & Blasi, P. 2006, MNRAS, 371, 1251
Amato, E., & Blasi, P. 2009, MNRAS, 392, 1591
Axford, W. I., Leer, E., & Skadron, G. 1978, ICRC (Budapest), 11, 132
Bai, X.-N., Caprioli, D., Sironi, L., & Spitkovsky, A. 2015, ApJ, 809, 55
Bai, X.-N., Ostriker, E. C., Plotnikov, I., & Stone, J. M. 2019, ApJ, 876, 60
Ballet, J. 2006, AdSpR, 37, 1902
Bamba, A., Yamazaki, R., Yoshida, T., Terasawa, T., & Koyama, K. 2005, ApJ, 621, 793
Baring, M. G., Ellison, D. C., & Jones, F. C. 1995, AdSpR, 15, 397
Bell, A. R. 1978, MNRAS, 182, 147
Bell, A. R. 1987, MNRAS, 225, 615
Bell, A. R. 2004, MNRAS, 353, 550
Bell, A. R., Matthews, J. H., & Blundell, K. M. 2019, MNRAS, 488, 2466
Bell, A. R., Schure, K. M., & Reville, B. 2011, MNRAS, 418, 1208
Bennett, L., & Ellison, D. C. 1995, JGR, 100, 3439
Berezhko, E. G., & Ellison, D. C. 1999, ApJ, 526, 385
Berezhko, E. G., & Völk, H. J. 1997, APh, 7, 183
Berezhko, E. G., & Völk, H. J. 2004, A&A, 427, 525
Berezhko, E. G., & Völk, H. J. 2006, A&A, 451, 981
Blandford, R., & Eichler, D. 1987, PhR, 154, 1
Blandford, R. D., & Ostriker, J. P. 1978, ApJL, 221, L29
Blasi, P. 2002, APh, 16, 429
Blasi, P. 2004, APh, 21, 45
Blasi, P., Amato, E., & Serpico, P. D. 2012, PhRvL, 109, 061101
Bret, A. 2020, ApJ, 900, 111
Burgess, D., Hellinger, P., Gingell, I., & Trávníček, P. M. 2016, JPlPh, 82, 905820401
Burgess, D., Lucek, E. A., Scholer, M., et al. 2005, SSRv, 118, 205
Bykov, A. M., Brandenburg, A., Malkov, M. A., & Osipov, S. M. 2013, SSRv, 178, 201
Caprioli, D. 2011, JCAP, 5, 26
Caprioli, D. 2012, JCAP, 7, 38
Caprioli, D. 2015, ICRC (The Hague), 34, 8
Caprioli, D., Amato, E., & Blasi, P. 2010, APh, 33, 160
Caprioli, D., Blasi, P., & Amato, E. 2009a, MNRAS, 396, 2065
Caprioli, D., Blasi, P., Amato, E., & Vietri, M. 2008, ApJL, 679, L139
Caprioli, D., Blasi, P., Amato, E., & Vietri, M. 2009b, MNRAS, 395, 895
Caprioli, D., & Haggerty, C. 2019, ICRC (Madison, WI), 36, 209
Caprioli, D., Haggerty, C. C., & Blasi, P. 2020, ApJ,
Caprioli, D., Pop, A., & Spitkovsky, A. 2015, ApJL, 798, 28
Caprioli, D., & Spitkovsky, A. 2013, ApJL, 765, L20
Caprioli, D., & Spitkovsky, A. 2014a, ApJ, 783, 91
Caprioli, D., & Spitkovsky, A. 2014b, ApJ, 794, 46

Caprioli, D., & Spitkovsky, A. 2014c, ApJ, 794, 47
Caprioli, D., Yi, D. T., & Spitkovsky, A. 2017, PhRvL, 119, 171101
Caprioli, D., Zhang, H., & Spitkovsky, A. 2018, JPlPh, 84, 715840301
Caprioli, D., et al. 2010, MNRAS, 407, 1773
Cassam-Chenaï, G., Hughes, J. P., Reynoso, E. M., Badenes, C., & Moffett, D. 2008, ApJ, 680, 1180
Chevalier, R. A., & Fransson, C. 2006, ApJ, 651, 381
Chevalier, R. A., & Raymond, J. C. 1978, ApJL, 225, L27
Crumley, P., Caprioli, D., Markoff, S., & Spitkovsky, A. 2019, MNRAS, 485, 5105
Drury, L. O'C. 1983, RPPh, 46, 973
Drury, L. O'C., & Völk, H. J. 1981a, ApJ, 248, 344
Drury, L. O'C., & Völk, H. J. 1981b, in IAU Symp. 94, Origin of Cosmic Rays: Shock Structure Including Cosmic Ray Acceleration (Dordrecht: D. Reidel), 363
Eichler, D. 1979, ApJ, 229, 419
Eichler, D. 1984, ApJ, 277, 429
Eichler, D. 1985, ApJ, 294, 40
Ellison, D. C., Baring, M. G., & Jones, F. C. 1995, ApJ, 453, 873
Ellison, D. C., Baring, M. G., & Jones, F. C. 1996, ApJ, 473, 1029
Ellison, D. C., & Double, G. P. 2002, APh, 18, 213
Ellison, D. C., & Eichler, D. 1984, ApJ, 286, 691
Ellison, D. C., & Eichler, D. 1985, PhRvL, 55, 2735
Ellison, D. C., Jones, F. C., & Eichler, D. 1981, JGZG, 50, 110
Ellison, D. C., Moebius, E., & Paschmann, G. 1990, ApJ, 352, 376
Gargaté, L., Bingham, R., Fonseca, R. A., & Silva, L. O. 2007, CoPhC, 176, 419
Gargaté, L., Fonseca, R. A., Niemiec, J., et al. 2010, ApJL, 711, L127
Gargaté, L., & Spitkovsky, A. 2012, ApJ, 744, 67
Ghavamian, P., Laming, J. M., & Rakowski, C. E. 2007, ApJL, 654, L69
Giacalone, J. 2004, ApJ, 609, 452
Giacalone, J., Burgess, D., Schwartz, S. J., & Ellison, D. C. 1992, GeoRL, 19, 433
Giacalone, J., Burgess, D., Schwartz, S. J., & Ellison, D. C. 1993, ApJ, 402, 550
Giacalone, J., Burgess, D., Schwartz, S. J., Ellison, D. C., & Bennett, L. 1997, JGR, 102, 19789
Giacalone, J., & Ellison, D. C. 2000, JGR, 105, 12541
Gieseler, U. D. J., Jones, T. W., & Kang, H. 2000, A&A, 364, 911
Guo, F., & Giacalone, J. 2013, ApJ, 773, 158
Haggerty, C., Caprioli, D., & Zweibel, E. 2019, ICRC (Madison, WI), 36, 279
Haggerty, C. C., & Caprioli, D. 2019, ApJ, 887, 165
Hanusch, A., Liseykina, T. V., Malkov, M., & Aharonian, F. 2019, ApJ, 885, 11
Jones, F. C., & Ellison, D. C. 1991, SSRv, 58, 259
Jones, F. C., Lukasiak, A., Ptuskin, V., & Webber, W. 2001, ApJ, 547, 264
Kang, H., & Jones, T. W. 2005, ApJ, 620, 44
Kang, H., & Jones, T. W. 2006, APh, 25, 246
Kang, H., Jones, T. W., & Edmon, P. P. 2013, ApJ, 777, 25
Kang, H., Jones, T. W., & Gieseler, U. D. J. 2002, ApJ, 579, 337
Kang, H., & Ryu, D. 2018, ApJ, 856, 33
Kirk, J. G., Duffy, P., & Gallant, Y. A. 1996, A&A, 314, 1010
Knežević, S., Läsker, R., van de Ven, G., et al. 2017, ApJ, 846, 167
Kropotina, Y. A., Bykov, A. M., Krasil'shchikov, A. M., & Levenfish, K. P. 2016, JTePh, 61, 517
Krymskii, G. F. 1977, DoSSR, 234, 1306
Kulsrud, R., & Pearce, W. P. 1969, ApJ, 156, 445
Lipatov, A. S. 2002, The Hybrid Multiscale Simulation Technology: an Introduction with Application to Astrophysical and Laboratory Plasmas (Berlin: Springer)
Lucek, S. G., & Bell, A. R. 2000, MNRAS, 314, 65
Malkov, M. A. 1997, ApJ, 485, 638
Malkov, M. A., Diamond, P. H., & Völk, H. J. 2000, ApJL, 533, L171
Malkov, M. A., & Drury, L. O'C. 2001, RPPh, 64, 429
Malkov, M. A., & Völk, H. J. 1996, ApJ, 473, 347
Margutti, R., Metzger, B. D., Chornock, R., et al. 2019, ApJ, 872, 18
Miceli, M., Bocchino, F., Decourchelle, A., et al. 2012, A&A, 546, A66
Morlino, G., Amato, E., Blasi, P., & Caprioli, D. 2010, MNRAS, 405, L21
Morlino, G., Blasi, P., Bandiera, R., Amato, E., & Caprioli, D. 2013, ApJ, 768, 148
Morlino, G., Blasi, P., & Vietri, M. 2007, ApJ, 658, 1069
Morlino, G., & Caprioli, D. 2012, A&A, 538, A81
Parizot, E., et al. 2006, A&A, 453, 387
Quest, K. B. 1988, JGR, 93, 9649
Ressler, S. M., et al. 2014, ApJ, 790, 85
Reville, B., & Bell, A. R. 2012, MNRAS, 419, 2433
Reville, B., & Bell, A. R. 2013, MNRAS, 430, 2873
Reville, B., Kirk, J. G., Duffy, P., & O'Sullivan, S. 2008, IKMPD, 17, 1795
Reynoso, E. M., Hughes, J. P., & Moffett, D. A. 2013, AJ, 145, 104
Riquelme, M. A., & Spitkovsky, A. 2009, ApJ, 694, 626
Sarbadhicary, S. K., Badenes, C., Chomiuk, L., Caprioli, D., & Huizenga, D. 2017, MNRAS, 464, 2326
Scholer, M. 1990, GeoRL, 17, 1821
Scholer, M., & Belcher, J. W. 1971, SoPh, 16, 472
Skilling, J. 1975, MNRAS, 172, 557
Slane, P., Lee, S.-H., Ellison, D. C., et al. 2014, ApJ, 783, 33
Tatischeff, V., & Hernanz, M. 2007, ApJL, 663, L101
Tran, A., Williams, B. J., Petre, R., Ressler, S. M., & Reynolds, S. P. 2015, ApJ, 812, 101
Uchiyama, Y., Aharonian, F. A., Tanaka, T., Takahashi, T., & Maeda, Y. 2007, Natur, 449, 576
Vainio, R., & Schlickeiser, R. 1999, A&A, 343, 303
van Marle, A. J., Casse, F., & Marcowith, A. 2018, MNRAS, 473, 3394
Vladimirov, A., Ellison, D. C., & Bykov, A. 2006, ApJ, 652, 1246
Völk, H. J., Berezhko, E. G., & Ksenofontov, L. T. 2005, A&A, 433, 229
Völk, H. J., & McKenzie, F. J. 1981, ICRC (Bangalore), 9, 287
Warren, J. S., et al. 2005, ApJ, 634, 376
Winske, D. 1985, SSRv, 42, 53
Winske, D., & Omidi, N. 1996, JGR, 101, 17287
Zacharegkas, G., Caprioli, D., & Haggerty, C. 2019, ICRC (Madison, WI), 36, 483
Zachary, A. L., & Cohen, B. I. 1986, JCoPh, 66, 469
Zirakashvili, V. N., & Aharonian, F. A. 2010, ApJ, 708, 965
Zirakashvili, V. N., & Ptuskin, V. S. 2008, in AIP Conf. Proc. 1085, High Energy Gamma-Ray Astronomy (Heidelberg: AIP), 336
Zirakashvili, V. N., Ptuskin, V. S., & Völk, H. J. 2008, ApJ, 678, 255
Zweibel, E. G. 2003, ApJ, 587, 625